

Advantages of fiber Bragg gratings for measuring electric motor loadings in aerospace application

Cite as: Rev. Sci. Instrum. **90**, 075005 (2019); <https://doi.org/10.1063/1.5093556>

Submitted: 21 February 2019 . Accepted: 08 July 2019 . Published Online: 31 July 2019

Douglas Keller , Daniel R. Eagan , Gilberto J. Fochesatto, Rorik Peterson, Hon Man Chan, and Allen Parker



View Online



Export Citation



CrossMark




NEW

AVS Quantum Science

A high impact interdisciplinary journal for **ALL** quantum science



ACCEPTING SUBMISSIONS

Advantages of fiber Bragg gratings for measuring electric motor loadings in aerospace application

Cite as: Rev. Sci. Instrum. 90, 075005 (2019); doi: 10.1063/1.5093556

Submitted: 21 February 2019 • Accepted: 8 July 2019 •

Published Online: 31 July 2019



Douglas Keller, Jr.,^{1,a)} Daniel R. Eagan,¹ Gilberto J. Fochesatto,^{2,b)} Rorik Peterson,^{1,c)} Hon Man Chan,^{3,d)} and Allen Parker^{3,e)}

AFFILIATIONS

¹Department of Mechanical Engineering, College of Engineering and Mines, University of Alaska Fairbanks, Fairbanks, Alaska 99709, USA

²Geophysical Institute, University of Alaska Fairbanks, Fairbanks, Alaska 99775, USA

³Armstrong Flight Research Center, National Aeronautics and Space Administration, Edwards, California 93523, USA

^{a)}dg.kllrjr@gmail.com. URL: <https://dkllrjr.github.io>.

^{b)}gjfochesatto@alaska.edu

^{c)}rapeterson@alaska.edu

^{d)}hon.chan@nasa.gov

^{e)}allen.r.parker@nasa.gov

ABSTRACT

Electric motors are being investigated in-depth for their application in aerospace. Part of this investigation is the characterization of the loadings from the propulsion devices, in a stationary setup, usually accomplished through the utilization of load cells. The majority of the load cells used in this application are designed around a resistance-based strain gauge. However, electric motors radiate electromagnetic interference (EMI) when in operation, which degrades the signal retrieved through the strain gauge, due to the gauge's metallic construction acting as an antenna for the EMI. To demonstrate the advantage of fiber Bragg gratings (FBGs), with their immunity to EMI, a load cell implementing both sensor technologies was designed and subjected to the same mechanical loading and EMI, with a flywheel coupled to a brushless DC motor. The load cell had a sensitivity of 8.59 ± 0.18 N and 2.49 ± 2.49 N through the strain gauge and FBG system, respectively. The strain gauge signal contained the mechanical loading signal embedded in wideband noise and spikes (that increased linearly with motor angular velocity), while the FBG signal did not, with little noise. The raw strain gauge signal, at a maximum, had a signal power ratio (mechanical signal power divided by the overall signal power mean) of 21.06 at 104.72 rad/s; the FBG signal, at a minimum, had a signal power ratio of 40.09 at 52.36 rad/s. Therefore, on the basis of the mechanical tests performed in this work, the recommended sensor of choice for electric propulsion in aerospace applications is the FBG.

Published under license by AIP Publishing. <https://doi.org/10.1063/1.5093556>

I. INTRODUCTION

The increasing viability of electric propulsion for ground-based applications has prompted investigation into electric propulsion for aerospace. Part of this investigation involves the stationary testing and research of electric motors, such as with the NASA's Airvolt electric motor test stand.¹ NASA's Airvolt testing has determined problematic areas in data collection; one such area is the mitigation of electromagnetic interference (EMI; Fig. 1) emitted from the electric motors under testing. This EMI affects the fidelity of the sensors gathering data during testing. Some of the worst affected sensors are the load cells¹ used to collect the thrust and torque loadings created

by the motor. The load cells in the experiment used resistance-based strain gauges, commonly referred to as foil gauges (as they are etched from a metallic foil), which is the de facto standard for measuring strains in load sensing applications.

Foil gauges are sensors that change resistance with an applied strain.^{2,3} They are well known and commonly used in strain sensing applications and in commercially available load cells. They are generally described by a manufacturer supplied constant (responsivity), known as the gauge factor, GF ,

$$GF = \frac{\Delta R/R}{\epsilon}, \quad (1)$$

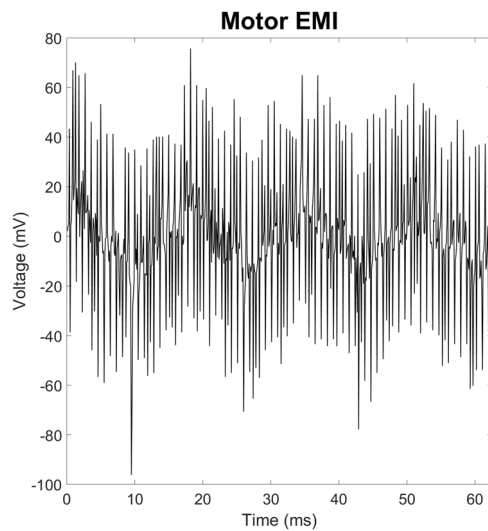


FIG. 1. The electromagnetic interference emitted by the Q100-5L motor when operated at 167.56 rad/s; it was collected with the Tektronix TDS3032B oscilloscope at a sampling rate of 10 kS/s, with the probe held next to, but not contacting, the strain sensors on the load cell. The collected signal resembles a series of spikes and cyclical noise due to the aliasing of the sampling frequency on the square waves energizing the coils of the motor.

where R is the resistance of the foil gauge and ΔR is the change in resistance due to the applied strain, ϵ . This can be arranged to focus on the strain,

$$\epsilon = \frac{\Delta R/R}{GF}. \quad (2)$$

To demonstrate the pervasion of the EMI in foil gauge signals, they are compared to the strain signals retrieved from a fiber Bragg grating (FBG). FBGs are etchings in a fiber optic cable, creating a sudden periodic change in the core refractive index.⁴⁻⁶ They reflect a particular wavelength, known as the Bragg, or resonance, wavelength, and transmit the rest when subjected to an optical input. When subjected to strain, the Bragg wavelength shifts proportionally, as described by the following equations:⁴⁻⁶

$$\lambda_{B,\epsilon} - \lambda_{B,0} = \Delta\lambda_B \approx 0.78\lambda_{B,0}\epsilon, \quad (3)$$

and rearranging for strain,

$$\epsilon \approx \frac{\Delta\lambda_B}{0.78\lambda_{B,0}}, \quad (4)$$

where ϵ is the strain applied to the FBG, $\Delta\lambda_B$ is the shift in Bragg wavelength, $\lambda_{B,\epsilon}$ is the strained FBG Bragg (resonant) wavelength, and $\lambda_{B,0}$ is the unstrained FBG wavelength.

They are commonly used for distributed sensing as a single fiber can carry multiple FBGs. With this, they find application in areas such as monitoring structural health, where the fiber is embedded in concrete bars to monitor strain for potential cracking at multiple points.⁷ Depending on their arrangement, they can also be configured to measure pressure (sensitivity ≈ 12 pm/MPa), temperature (sensitivity ≈ 11.5 pm/ $^{\circ}$ C), or even acoustic waves, all of which are found in the oil industry.⁸ But their main purpose in this

paper is their immunity to EMI,⁴⁻⁶ which allows them to provide a true mechanical loading reference point to compare against the foil gauges.

EMI is the high frequency electromagnetic perturbation emitted from inadequately shielded electronics and/or electromechanical systems. These emissions interact with nearby electronics and can lead to performance degradation if not properly handled.⁹ Due to their metallic construction, foil gauges act as antennas and easily capture EMI. Since they must be in physical contact with the object where the strain is measured, this prevents standard ways of mitigating external noise, such as shielding, as the sensor cannot be completely surrounded in relation to the motor, and grounding, since this would result in the loss of the strain signal. In the case of brushless DC electric motors, a common form of electric motors in aerospace application experiments, the EMI manifests itself in the alternating voltage square waves resulting from energizing the motor stator coils. When these square waves are sampled at the rates used to measure mechanical loadings, as these are generally at lower frequencies than the square waves, they take the form found in Fig. 1. That is to say, the EMI at this sampling rate, 10 kS/s (S is samples and s is seconds), resembles a series of high frequency spikes and lower frequency cyclical noise because it is undersampled at this sampling rate.

To compare the foil gauge and FBG signals in the presence of EMI, they are collected through load cell measurements made while operating an electrical motor, designed for aerospace use, coupled to a flywheel for dynamic mechanical loading. However, currently there are no load cells commercially available that utilize FBGs for load measuring. This created a need to develop such a device for this experiment, resulting in a load cell with both foil gauges and an FBG implemented to measure strain. This design subjects both sensors to the same mechanical loading and EMI, allowing for the analysis of the results in terms of EMI contamination. In this way, this paper aims to convey the advantages of FBGs for load measurements produced by electric motors in aerospace application.

This paper is divided into the description of the test apparatus (Sec. II A), the design and calibration of the load cell (Sec. II B), and the mathematical methods utilized for the signal analysis (Sec. II C), followed by the results and discussion (Secs. III and IV).

II. METHODOLOGY

A. Test apparatus

The experimental setup is found in Fig. 2, with the instruments listed in Table I. The Q100-5L motor, coupled to a flywheel (arrangement in Fig. 3), is mounted to the load cell, which is affixed to the stationary test stand. The flywheel provides a known static axial weight for the load cell to sense. The foil gauges from the load cell are connected to a Wheatstone bridge in half-bridge arrangement, powered by a high precision and low drift Agilent 6614C DC power supply (required for accurate dynamic strain measurements), and is connected to the transimpedance Advanced Research Instruments DC-100 amplifier (DC to 100 MHz with low noise) to boost the Wheatstone bridge's small output voltage signal. This small signal is then sampled, digitized, and recorded by the Tektronix TDS3032B digital oscilloscope and transferred to the laptop computer through a high data rate Ethernet connection. The power supply, amplifier, and oscilloscope are all grounded to a common ground,

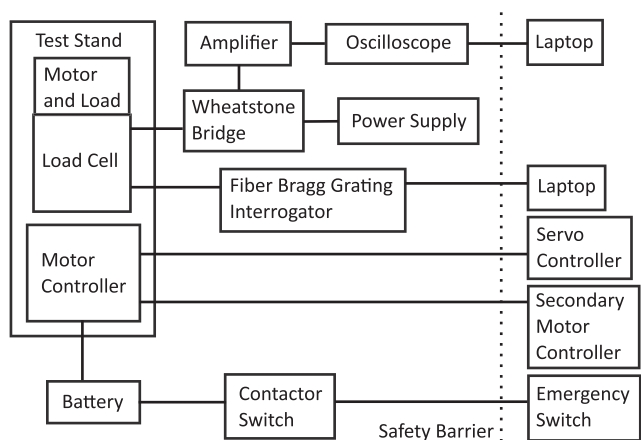


FIG. 2. The experimental setup and layout. The motor and flywheel (load), main motor controller, and load cell were mounted to the test stand. The collecting and control instruments were placed behind a safety barrier for safe operation and data acquisition. The motor was controlled by two motor controllers (main and secondary) and a servo controller for operation. Two laptops acquired the data for the FBG and the foil gauges, with their respective auxiliary instruments (interrogator and oscilloscope). The motor was powered by a battery, inline with an emergency switch.

removing the EMI from their respective circuits. The FBG from the load cell is interrogated by the NASA Fiber Optic Sensing System (FOSS), with the data transferred by Ethernet to a separate laptop computer.

The motor is controlled primarily by the JETI SPIN Pro 300 Opto motor controller, assisted by the secondary JETI JETIBOX controller. The main motor controller supplies the square wave to the motor coils, while the secondary controller regulates the ramping up of the power delivered to the motor. This was done to protect the motor and act as a current limiter during motor start-up. The motor's speed and operation are manually controlled by the HFP-30 servo controller. The MaxAmps 6s LiPo battery is connected to the main motor controller, powering the motor system. To comply with security and safety norms, a contactor switch in the path between the motor controller and the battery is powered by

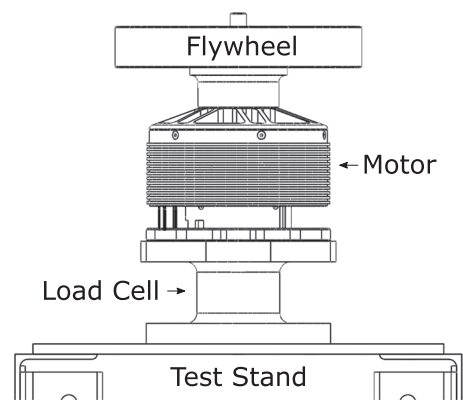


FIG. 3. Arrangement of the flywheel, motor, load cell, and test stand in the setup. The flywheel is bolted to the motor, the motor is bolted to the load cell, and the load cell is bolted to the test stand. This provides a path for the force to flow through the load cell.

an auxiliary emergency switch, providing a safeguard mechanism, in case the experiment needs to be halted for any reason.

B. Load cell design

The experiment required a load cell able to measure thrust (tensile force) up to 356 N, while withstanding a combined loading of 356 N of tensile force and 17 Nm of torque. The design of the load cell is a hollow cylinder with a wall thickness of 0.25 mm, with flanges for mounting on either end (see Fig. 4), and was machined from the aluminum alloy, 2024 T351. The load cell was designed for the eventual placement on a flight platform for in-flight testing and as thus had geometrical constraints for mounting, which were adhered to. The loading is applied to the top flange (for this experiment the electric motor mounts to top flange with 4 bolts), and the bottom flange is used to mount the load cell to a stationary test stand with 6 bolts (Fig. 3). This allows a path for the force to flow through the load cell, resulting in measurable strain.

The thrust is measured through the strain of the longitudinal axis. Two foil gauges are placed along the cylinder wall, one in vertical placement and the other in horizontal placement (see Fig. 4 for

TABLE I. The instruments used in the testing apparatus.

Item	Manufacturer and model
Flywheel	1961 Ford Falcon flywheel 9.71 kg 27.4 cm Ø
Brushless DC electric motor	Hacker motor Q100-5L 11 kW 28 poles
Motor controller	JETI SPIN Pro 300 Opto
Battery	MaxAmps lithium-polymer 10 900 mAh 6S 22.2 V
Servo controller	Hitec HFP-30
Secondary motor controller	JETI JETIBOX
Fiber Bragg grating interrogator	NASA FOSS
DC power supply	Agilent 6614C 0–100 V 0–0.5 A
Amplifier	Advanced Research Instruments Corp. DC-100
Oscilloscope	Tektronix TDS3032B
Laptops	Windows 10 OS, Windows 7 OS

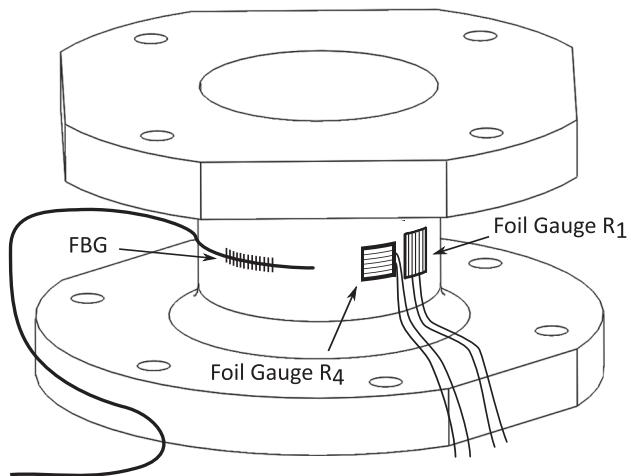


FIG. 4. The load cell design featuring a top 4 bolt flange, to mount to the motor, and a bottom 6 bolt flange, to mount to the test stand, and has a cylinder wall thickness of 0.25 mm. Two foil gauges, one vertical, R_1 , and one horizontal, R_4 , each with a resistance of 350 Ω , are placed on the cylinder wall. 2.54 cm away, an FBG is placed about the cylinder's curvature on the wall. The two foil gauges and FBG are equidistant from the bottom and top flanges.

sensor placement). An FBG is placed 2.54 cm from the two foil gauges, along the circumference of the cylinder wall, to measure the applied loading induced strain, and has a Bragg wavelength of 1550 nm. The foil gauges are in half-bridge arrangement in a Wheatstone bridge (see Fig. 7 and Sec. II B 2 a), which is powered by the power supply and measured by the oscilloscope, and the FBG is interrogated with the NASA FOSS (see Sec. II B 2 b).

1. Stress and strain analysis

For the load cell to retrieve the thrust, the cylinder is compressed or stretched along its longitudinal axis, resulting in a normal stress along this axis. The FBG and foil gauge placed horizontally along the circumference of the cylinder wall experience the imposed strain from the normal stress through Poisson's ratio [see Eq. (6)]. While this layout causes the FBG to experience about a third of the normal stress (with $\nu = 0.33$) along its length, this arrangement is required due to the minimum bending radius of the fiber optic cable, 25 mm (to prevent signal loss), which would interfere with the load cell flanges if placed vertically (shaped as such due to the aforementioned geometric constraints). The vertically placed foil gauge experiences the strain from the normal stress directly [see Eq. (5)]. To calculate the thrust from the measurement, the strain is related to the force acting on the cross section with the following equations:^{10,11}

$$\varepsilon_v = \frac{\sigma}{E} = \frac{P}{AE}, \quad (5)$$

$$\varepsilon_h = \nu \varepsilon_v, \quad (6)$$

where ε_v is the measured strain from the vertically mounted foil gauge and ε_h is the measured strain from the horizontally mounted sensors. σ is the normal stress imposed by the force (thrust) P , with the given cylinder cross-sectional area, A . ν and E are Poisson's ratio and elastic modulus of the load cell material, respectively

TABLE II. The mechanical properties of aluminum 2024 T351.¹²

Elastic modulus, E (GPa)	73.77
Poisson's ratio, ν	0.33
Thermal expansion coefficient, α ($^{\circ}\text{C}^{-1}$)	22.41×10^{-6}
Yield stress (MPa)	358.5
Infinite cyclic fatigue limit (MPa)	76.5

(see Table II for the properties of aluminum 2024 T351). The calculated vertical strain and horizontal strain are 118.4×10^{-6} and 39.1×10^{-6} of elongation, respectively, for the applied loading of 356 N. Although stress concentrations at the mounting holes and fillets are present, the constant cross section of the main cylinder area, where the strain measuring sensors are mounted, is not affected by this, therefore producing a uniform strain.

The aluminum yield stress and cyclic fatigue limit in Table II impose constraints for the maximum loading applicable to the load cell. To remain in the elastic range, the experienced stress needs to remain below 358.5 MPa, and to endure infinite cyclic loadings, it needs to remain below 76.5 MPa. With the expected maximum combined loading of 356 N and 17 Nm, the maximum possible experienced stress in the material needed to be determined. For this, the von Mises stress, which is applicable to ductile materials such as aluminum,¹³ was utilized. The von Mises stress in a plane can be solved with the following relation:¹³

$$\sigma_{vM} = \sqrt{\sigma^2 + 3\tau^2}, \quad (7)$$

where σ_{vM} is the maximum stress experienced or the von Mises stress. σ is the normal stress applied, mentioned earlier, and τ is the shear stress applied and is determined by the following:^{10,11}

$$\tau = \frac{Tr}{J}, \quad (8)$$

where T is the applied torque loading, r is the outer radius of the cylinder wall, and J is the polar moment of inertia about the longitudinal axis. The forces and stresses are labeled in Fig. 5. With the given maximum expected loadings, σ_{vM} was found

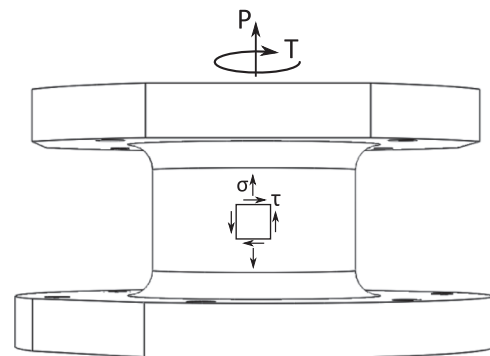


FIG. 5. The load cell design with a small plane unit square on the cylinder wall, labeling the normal, σ , and shear, τ , stresses. P is the applied thrust, and T is the applied torque.

to be 29.65 MPa, well below the yield stress and comfortably below the infinite cyclic fatigue limit. Consequently, the maximum thrust load, without torque, constrained by the fatigue limit is 3118 N.

To confirm the theoretical calculations, simulations in SolidWorks were performed. The simulation results matched those found analytically. SolidWorks calculated, with the given maximum loadings, σ_{VM} to be 29.51 MPa, practically the same as the analytical result. Figure 6 shows the strain in the vertical direction from the simulations. A uniform stress/strain appears on the cylinder of load cell, confirming the previous assumption that the geometrical stress concentrations at the mounting points do not reach the area with the sensors.

2. Strain measurement

The characteristics of the foil gauges and FBG are found in Table III. Both sensors were affixed to the load cell cylinder wall with cyanoacrylate glue; then, the free hanging wires/cables were secured to the test stand with tape to prevent movement during motor operation.

a. Wheatstone bridge. To determine the small resistance change in the strained foil gauges, a Wheatstone bridge circuit was used (Fig. 7). A half-bridge arrangement was chosen for the circuit design, with R_1 and R_4 as the two foil gauges present on the load cell (refer back to Fig. 4). R_1 and R_4 are the vertically and horizontally mounted gauges, respectively. R_2 and R_3 are 330 Ω resistors, and R_p is a precision potentiometer of 100 Ω to balance the bridge.

Both gauges experience the same strain, ϵ_v , but R_4 experiences the strain due to Poisson's ratio, ϵ_h , or $\nu\epsilon_v$. The change in the balanced bridge output voltage due to an induced strain on the gauges

TABLE III. The foil gauge and fiber Bragg grating characteristics.

Foil gauge	
Manufacturer	Micro-Measurement
Gauge factor, GF (%)	2.105 ± 0.5
Resistance, R (Ω)	350.0 ± 1.05
Transverse sensitivity (%)	0.7
Gauge width (mm)	3.175
Gauge length (mm)	3.175
Fiber Bragg grating	
Manufacturer	NASA Armstrong FOSS Lab
Grating	Uniform
Length (mm)	6
Reflectivity (%)	10
Bragg wavelength (nm)	1550

then can be described as follows:^{2,3}

$$\Delta V_o = \frac{GF(1 + \nu)\epsilon_v}{4} V_s, \quad (9)$$

where ΔV_o is the change in bridge output voltage and V_s is the bridge excitation voltage. GF is the gauge factor of the foil gauges described in Eq. (2). ϵ_v is the applied strain in Eq. (5). The oscilloscope samples the amplified bridge response at 10 kS/s. With the motor operating at a maximum angular velocity of 40 revolutions/s (251.33 rad/s), this provides a suitable sampling rate to measure the dynamic loadings of the motor/flywheel.

b. NASA FOSS. NASA's FOSS is used to interrogate the FBG response. The FBG on the fiber reflects its Bragg wavelength, 1550 nm unstrained (Table III). The device excites the FBG by illuminating the sensing fiber with a Thorlabs super luminescent diode (a broadband light source centered at 1550 nm) and then measures the reflected resonant wavelength with the BaySpec optical spectrum analyzer (see Table IV for details). The peak of the wavelength, and its shift with strain [according to Eq. (4)], is returned from the system in binary form via Ethernet connection from the onboard Raspberry Pi. The system measures the wavelengths at 5 kHz, providing

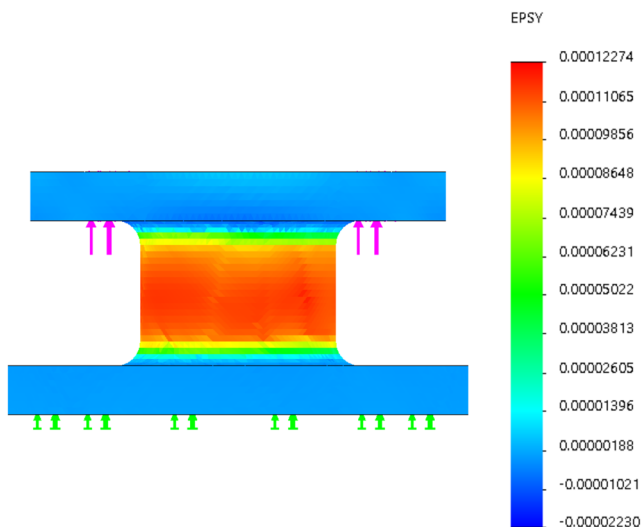


FIG. 6. The SolidWorks strain simulation of the resultant strain in the vertical direction, labeled EPSY in the figure. The maximum expected combined loading of 356 N and 17 Nm was used for the simulation. A clear, uniform strain is produced in the cylinder wall, demonstrating a reliable strain field for the sensors to measure.

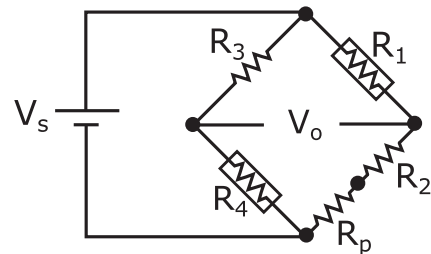


FIG. 7. The half-bridge Wheatstone bridge circuit used to measure the applied strain with the foil gauges. V_o is the bridge output voltage, and V_s is the bridge excitation voltage. R_1 and R_4 are the foil gauges (refer to Fig. 4 for sensor placement). R_p is the balancing potentiometer to zero the output voltage before testing. R_2 and R_3 are 330 Ω resistors to balance the foil gauge resistance.

TABLE IV. The NASA FOSS details.

Spectrum analyzer	
Manufacturer	BaySpec
Model	FBGA-F-1525-1565-FA
Resolution (pm)	1 ± 1
Sampling rate (kHz)	5
Light source	
Manufacturer	Thorlabs
Model	SLD1005S
Type	Super luminescent diode
Power (mW)	22
Center wavelength (nm)	1550
FWHM (nm)	50

a suitable sampling rate to measure the dynamic loadings present in the testing.

3. Calibration

The load cell was calibrated with an Instron Model 4400 tensile loading machine in a controlled environment laboratory. The load cell was quasistatically loaded in tension from 0 to 2224 N in roughly 22.24 N steps to produce a large data pool to assign a best fit linear regression model. Figure 8 shows the results of the model fitting. The FBG response is less variable, most likely due to the higher sensitivity provided by the NASA FOSS.

4. Sensitivity

The sensitivity of the strain measuring systems was determined utilizing Eqs. (4) and (9), with the instrument limitations. The Tektronix TDS3032B oscilloscope has a voltage measuring resolution of 1 mV and an accuracy of ± 0.02 mV. When backtracked through Eq. (9), the expected force resolution through the foil gauge system is 8.59 N, about 2.4% of the maximum expected loading of 356 N. NASA's FOSS has a wavelength measuring resolution of 1 pm and

TABLE V. Resolution of the two strain measurement systems on the load cell.

Foil gauges (N)	8.59 ± 0.18
Fiber Bragg gratings (N)	2.49 ± 2.49

an accuracy of ± 1 pm. When the load is solved for with Eq. (4), the force resolution is found to be 2.49 N, less than 1% of the expected maximum loading, demonstrating a better sensitivity than the foil gauge system due to the finer resolution of the FOSS than the oscilloscope in their respective systems. The sensitivities are tabulated in Table V.

C. Signal analysis

1. Despiking

As described in the Introduction, the EMI emitted from the motor is visualized in part as a series of high frequency spikes. These spikes are picked up by the foil gauges and are present in the signal. To characterize the mechanical loading signal from the foil gauges, it is necessary to detect and remove the signal spikes. To remove the spikes from, or despike, the foil gauge data, a moving median filter with a threshold is utilized.^{14,15} This median filter has a window size of $2N + 1$, where N is the filter order. The differences of the filter output and original data are then binned, forming a distribution. The first zero count bin away from the middle of the differences' distribution becomes the threshold. For the analysis here, a filter with the order of $N = 3$ was used with the bin count for each foil gauge signal recorded in Table VI.

2. Filtering

The lower frequency cyclical noise in the EMI is not removed with the despiking procedure. To further filter the despiked foil gauge signal, a Cauer bandpass filter was utilized on the frequency domain representation of the signal. The filter passed ± 5 Hz on either side of the recorded revolutions per second of the motor, where the motor-flywheel combination vibrated with the largest amplitude due to an imbalance in the flywheel. This vibration is

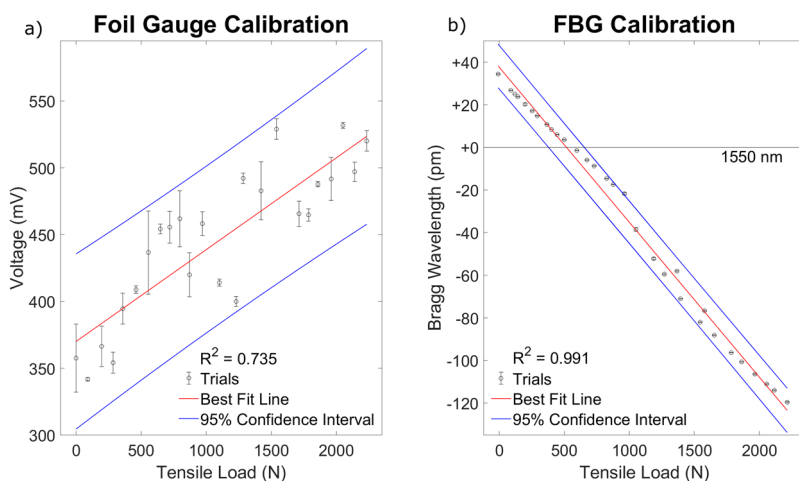


FIG. 8. The resulting calibration best fit lines, with the correlation coefficient, and 95% confidence intervals for the known linear response of both the foil gauge system (a) and FBG system (b). The measurement trials feature one standard error (standard error = σ/\sqrt{n} ; σ is the standard deviation and n is the number of measurements at each load) and length error bars for comparison.

TABLE VI. The despiking and time series filter specifications. The bin count for the despiking filter for each foil gauge signal, at the respective motor angular velocity.

Angular velocity (rad/s)	52.36	78.54	104.72	167.56	209.44	251.33
Despiking bin count	211	223	215	229	217	223

explained in greater detail in Sec. III. The rest of the filter details are found in Table VII.

D. Signal power ratio

To quantify the effectiveness of each strain measuring system, the signal power ratio (SPR) was calculated. This measures the strength of the mechanical loading signal in each dataset, compared to the rest of the signal. The SPR was calculated with the following formula:

$$SPR = 10 \log_{10} \left(\frac{P_{\text{loading}}}{\overline{P_{\text{signal}}}} \right). \quad (10)$$

With P_{loading} as the power of the mechanical loading signal and $\overline{P_{\text{signal}}}$ as the mean power of the entire signal, both retrieved from the frequency domain representation of the signal. The mechanical loading is taken as the loading caused by the vibration of the motor-flywheel combination mentioned previously.

E. Testing procedure

Noting the FBG's sensitivity to both strain and temperature,^{6,8,16} the experiment was performed in an environmentally controlled laboratory to provide a stable, constant temperature environment. In addition, the temperature of the motor was monitored through the JETI JETIBOX secondary motor controller to confirm the motor dissipated heat and remained at room temperature as it was the only source of heat with the potential to affect the FBG sensor. These methods, and the following procedure, allowed for the ability to assume the temperature remained constant during the testing and, therefore, the FBG signal was only affected by the change in strain.

TABLE VIII. The angular velocities the motor was operated at.

Angular velocity (rad/s)	52.36	78.54	104.72	167.56	209.44	251.33
--------------------------	-------	-------	--------	--------	--------	--------

The testing was conducted with the following procedure:

1. The test apparatus was checked and confirmed to be setup and connected properly, with personnel behind the safety barrier.
2. Next, both the foil gauge and FBG measuring systems were initialized and began recording.
3. The Q100-5L motor was slowly ramped up to speed with the Hitec HFP-30 servo controller.
4. The motor was allowed to come to steady state for roughly 30 s before being powered down, with an overall run time of about a minute (to prevent heat build up).
5. Upon power down of the motor, it was allowed to rest about 10 min (with temperature monitoring) to prevent further heat build up that would carry over to the next test.

This procedure was repeated for 6 angular velocities, found in Table VIII.

III. RESULTS

As an extra precaution for temperature, and ease of processing in the frequency domain, the datasets were analyzed in 1 s windows. Because the JETI JETIBOX secondary motor controller limits the acceleration of the motor, only the 1 s windows in the steady state region of the motor operation were analyzed. The analysis was focused on the dynamic signal, as this is where the EMI is present in our signals, due to its periodic nature (refer back to Fig. 1).

Both the high frequency spikes and wideband, low amplitude noise in Fig. 1 appear in the foil gauge signal. A quarter second window of both the EMI and the foil gauge signal (though not collected simultaneously) is shown in Figs. 9(a) and 9(b), respectively, demonstrating the resemblance. The spikes show the main connection of the EMI to the foil gauge signal, which were labeled and removed with the despiking process. The spikes appear in the signal

TABLE VII. The Cauer bandpass filter specifications used to filter the frequency domain representation of the foil gauge signal, per angular velocity of the motor, in both radians per second and revolutions per second. The filter passband is centered on the revolutions per second of the motor angular speed.

Angular velocity		Passband frequencies (Hz)		Stop band frequencies (Hz)	
rad/s	rev/s	Low	High	Low	High
52.36	8.33	3.33	13.33	2.81	792.24
78.54	12.5	7.5	17.5	6.32	799.75
104.72	16.67	11.67	21.67	9.84	803.27
167.56	26.67	21.67	31.67	18.27	811.7
209.44	33.33	28.33	38.33	23.89	817.32
251.33	40	35	45	29.51	822.94
		Passband ripple (dB)		Stop band attenuation (dB)	
All		0.1		60	

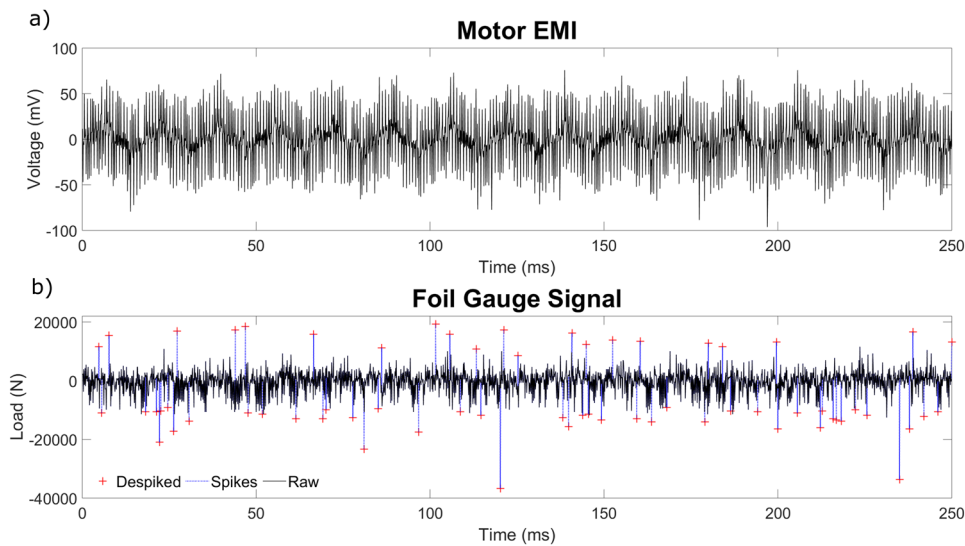


FIG. 9. (a) The motor EMI (same as Fig. 1) and (b) foil gauge signal with the motor running at 167.56 rad/s with the flywheel load. The raw and despiked signal, with removed spikes overlaid, is shown for the foil gauge system.

and increase in occurrence with increasing motor angular velocity, which is conveyed in Fig. 10 and Table IX. This relationship is linear, with a correlation coefficient of 0.938, which is expected as the alternating square waves supplied to the motor increase linearly with motor angular velocity. The linear increase of spikes per second with the linear increase in motor angular velocity demonstrates the connection between the foil gauge signal and the EMI.

The main mechanical loading was caused by the flywheel, which, although factory balanced, was still slightly out of balance, resulting in it tilting about its rotating axis while the motor ran. This tilting induced a vibration in the strain signals, as the cylinder load

cell began to act as a bending beam along the longitudinal axis. A perfectly balanced flywheel would result with a constant 127 N in the signal, including the motor weight. However, as the motor spun, the sensors are subjected to compression and tension in a cyclical fashion. This created a harmonic response about the static 127 N load of the flywheel/motor combination on the load cell and is visible in Fig. 11(a). The vibration matched perfectly to the motor revolutions per second, which is confirmed with the maximum peak of the FBG signal in the frequency domain [Fig. 11(b)].

The lower frequency noise from the EMI in the foil gauge signal, however, makes extracting the mechanical loading signal impossible without the further bandpass filtering. This noise, which is persistent after the despiking process, overshadows the mechanical loading to the point where the mechanical signal cannot be distinguished in the foil gauge signal. This is demonstrated in Fig. 12(a). The filtered foil gauge frequency domain series shows a peak at the motor revolutions per second [Fig. 12(b)] and appears as a harmonic response in the time domain [Fig. 12(a)].

The foil gauge signal found in Fig. 9 resembles the motor EMI much more than it does the FBG signal, which is considered the true mechanical signal. The SPR for each signal set is presented in Table X to show the effect of the EMI on the foil gauges. The SPR for the raw and despiked foil gauge signals is much lower than the bandpass filtered signals and the FBG signals. However, it must be noted that the centered frequency of which the bandpass filter is dependent upon to accurately filter the signals was only accessible due to the clarity of the mechanical loading signal in the FBG signals. Without this information, the bandpass filter could not be applied with any confidence to reveal any underlying mechanical signals. The need for the bandpass filter comes from the presence of EMI in the foil gauge signals. This is expected, given the pervasiveness of the EMI in the raw foil gauge signals and the lack of EMI in the FBG signals.

The FBG signals experience none of the issues related to EMI that the foil gauge signals do. There are no spikes or lower frequency cyclic noise present. Again, this is due to the inherent nature of the

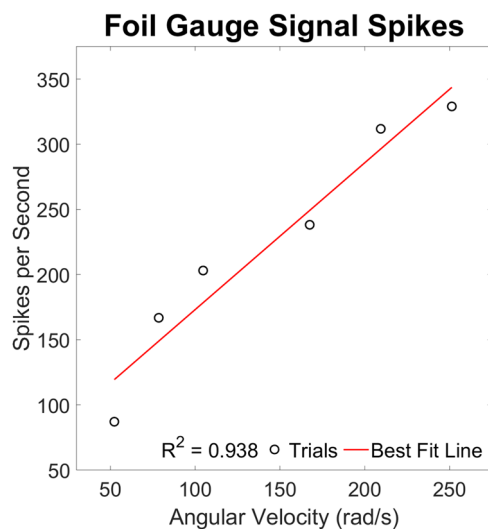
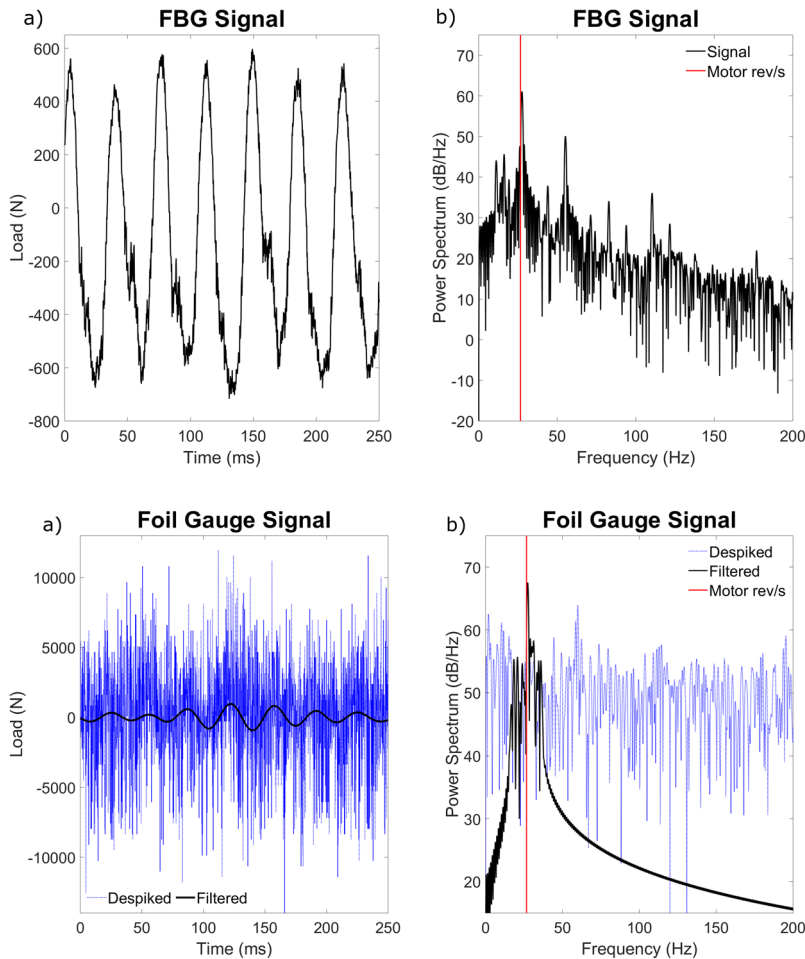


FIG. 10. The average spikes per second at the different motor operating speeds while under flywheel loading in the foil gauge signal. There is a distinct linear increase of spikes with increasing motor angular velocity, shown by the linear best fit line and correlation coefficient.

TABLE IX. The average spikes per second from the motor EMI in the foil gauge signal at the corresponding motor angular velocities with the flywheel loading, as seen in Fig. 10.

Angular velocity (rad/s)	52.36	78.54	104.72	167.56	209.44	251.33
Spikes per second	87.1	166.8	203.1	238.2	311.8	329.0

**FIG. 11.** The fiber Bragg grating signal with the motor operating at 167.56 rad/s: (a) the time series signal and (b) the frequency domain representation of the signal. The frequency series has the motor speed in revolutions per second overlaid.**FIG. 12.** The foil gauge response with the motor operating at 167.56 rad/s, both the despiked and filtered versions: (a) the time series signal and (b) the frequency domain representation of the signal. A Causer bandpass filter with a frequency window of 10 Hz, centered around the motor revolution per second speed (overlaid) was used to filter the signal. More filter specifications are found in Table VII.

FBG system with its immunity to EMI. The FBG signal requires no filtering to provide the mechanical loading data discernibly and even reveals the presence of different vibrational modes of the test apparatus structure (due to the motor/load cell arrangement or test stand

and are not investigated here), albeit at lower powers in the frequency domain [the lower peaks in Fig. 11(b)]. These are swallowed up in the noise in the foil gauge signals. This means the FBG more effectively measure the mechanical loading signal.

TABLE X. The signal power ratio of the mechanical loading signal power to the entire signal power [Eq. (10)], for all the signal datasets at the corresponding motor angular velocities.

Angular velocity (rad/s)	52.36	78.54	104.72	167.56	209.44	251.33
Foil gauge signal raw	15.79	12.95	21.06	15.73	14	11.24
Foil gauge signal despiked	15.62	14.31	22.47	17.66	16.53	13.57
Foil gauge signal filtered	86.24	76.53	87.69	90.68	84.27	74.56
Fiber Bragg grating signal	40.09	47.42	57.87	52.22	55.89	56.43

IV. DISCUSSION

In this testing, we compared the foil gauges against the fiber Bragg gratings to demonstrate the advantages of using FBGs for measuring mechanical loadings in an environment filled with electromagnetic interference created by a brushless DC motor made for aerospace application. The data show that the undersampled alternating square waves energizing the motor coils appear as spikes and wideband, low amplitude noise in the foil gauge signals, as the spikes increase linearly with increasing motor angular velocity. The spikes and cyclic noise are not present in the FBG signals at all, which instead shows a clear harmonic signal produced by the imbalanced flywheel, as it causes both gauge systems to experience compression and tension cyclically. This benefit is quantified by its high SPR, which is only surpassed by the bandpass filtered foil gauge signals, which depend on the FBG results to effectively implement. For the foil gauge system, the foil gauges act as antennas, picking up the EMI along with the strain signal. The EMI is unavoidable as the foil gauges must be in contact with the strained surface to experience the strain, preventing adequate shielding from being an option, and they cannot be grounded as that would lose the strain signal in terms of voltage in the Wheatstone bridge circuit. For applications relatively free of EMI, or in applications where the EMI can be effectively mitigated prior to strain measurement, foil gauges operate well, as seen by the calibration tests performed here. However, from the perspective of the experimental results, when measuring strain, and therefore mechanical loadings, in an environment filled with EMI, the FBGs are better suited for the application.

With the prevalence of electrical motors in the ground transportation industry, the drive to bring this method of propulsion to aerospace is increasing. However, to do this, safe stationary testing first needs to be performed to characterize it. The challenge that electric motors bring to this research is their emittance of EMI, which affects sensing systems in ways that prior methods of propulsion did not.¹ Therefore, as the research continues in this direction, fiber Bragg gratings are the sensor of choice to effectively measure mechanical loadings surrounded by electromagnetic interference.

ACKNOWLEDGMENTS

The authors would like to thank NASA Armstrong, particularly the NASA Armstrong FOSS Lab, for providing the funding

and hardware for this project. The authors would also like to thank NASA Armstrong engineers James Murray and Paul Bean for their expertise and collaboration through this joint venture and to thank Cheng-fu Chen, Professor of Mechanical Engineering at the University of Alaska Fairbanks (UAF), for his comments and insight on this project. D. Keller and D. Eagan would also like to recognize the independent support provided by the UAF Undergraduate Research and Scholarly Activity program.

REFERENCES

- ¹A. Samuel and Y. Lin, in *51st AIAA/SAE/ASEE Joint Propulsion Conference* (AIAA, Orlando, Florida, 2015).
- ²R. S. Figliola and D. E. Beasley, *Theory and Design for Mechanical Measurements*, 5th ed. (John Wiley & Sons, Inc., Hoboken, New Jersey, 2011).
- ³J. W. Dally and W. F. Riley, *Experimental Stress Analysis*, 3rd ed. (College House Enterprises, LLC, Knoxville, Tennessee, 1991).
- ⁴A. D. Kersey, M. A. Davis, H. J. Patrick, M. LeBlanc, K. P. Koo, C. G. Askins, M. A. Putnam, and E. J. Friebele, *J. Lightwave Technol.* **15**, 1442 (1997).
- ⁵B. Lee, *Opt. Fiber Technol.* **9**, 57 (2003).
- ⁶D. Krohn, T. MacDougall, and A. Mendez, *Fiber Optic Sensors: Fundamentals and Applications*, 4th ed. (Society of Photo-Optical Instrumentation Engineers, Bellingham, Washington, 2014).
- ⁷M. Majumder, T. K. Gangopadhyay, A. K. Chakraborty, K. Dasgupta, and D. Bhattacharya, *Sens. Actuators, A* **147**, 150 (2008).
- ⁸X. Qiao, Z. Shao, W. Bao, and Q. Rong, *Sensors* **17**, 429 (2017).
- ⁹H. W. Ott, *Noise Reduction Techniques in Electronic Systems*, 2nd ed. (John Wiley & Sons, Inc., New York, 1988).
- ¹⁰R. Solecki and R. J. Conant, *Advanced Mechanics of Materials* (Oxford University Press, New York, 2003).
- ¹¹S. P. Timoshenko and J. N. Goodier, *Theory of Elasticity* (McGraw-Hill, Inc., New York, 1970).
- ¹²R. C. Rice, J. L. Jackson, J. Bakuckas, and S. Thompson, "Metallic materials properties development and standardization," RES Report DOT/FAA/AR-MMPDS-01, Federal Aviation Administration, U.S. Department of Transportation, 2003.
- ¹³R. C. Juvinall and K. M. Marshek, *Fundamentals of Machine Component Design*, 5th ed. (John Wiley & Sons, Inc., Hoboken, New Jersey, 2012).
- ¹⁴F. V. Brock, *J. Atmos. Oceanic Technol.* **3**, 51 (1986).
- ¹⁵D. Starkenburg, S. Metzger, G. J. Fochesatto, J. G. Alfieri, R. Gens, A. Prakash, and J. Cristobal, *J. Atmos. Oceanic Technol.* **33**, 2001 (2016).
- ¹⁶D. A. Krohn, *Fiber Optic Sensors: Fundamentals and Applications*, 2nd ed. (Instrument Society of America, Research Triangle Park, North Carolina, 1992).